

Thermal Transient Characterization Methodology for Single-Chip and Stacked Structures

Oliver Steffens², Péter Szabó¹, Michael Lenz³, Gábor Farkas¹
¹MicReD Ltd., Budapest XI, Gulyás u. 27, H-1112 Hungary,
 e-mail: <szabop | farkas>@micred.com

²Infineon Technologies AG, Wernerwerkstrasse. 2, P.O. Box 10 09 44, D-93009 Regensburg, Germany

³Infineon Technologies AG, Balanstrasse 73, D-81541 München, Germany
 e-mail: <oliver.steffens | michael.lenz>@infineon.com

Abstract

High-power semiconductor packages typically exhibit a three-dimensional heat flow, resulting in large lateral changes in chip and case surface temperature. For single-chip devices we propose to use an unambiguous definition for the junction-to-case thermal resistance as a key parameter, based on a transient measurement technique with much higher repeatability also for very low thermal resistances compared to a two-point thermal resistance measurement. The technique is illustrated on thermal transient measurements of power MOSFETs. A comparison between different thermal coupling to the ambient is used to demonstrate the method's capability to reveal even subtle internal details of the package. The concept is extended to multichip and stacked-chip structures, where transfer impedances have to be introduced. Here, the dynamic properties of the package are important and complex impedance mapping is the proper way to characterize the package.

1. Introduction

For devices with a nearly perfect one-dimensional (1D) heat flow the junction-to-case thermal resistance is defined as

$$R_{thJC} = (T_J - T_C)/P \quad (1)$$

where T_J means the temperature of the junction at a certain powering, T_C the temperature of the case and P the power dissipated at the junction. This quantity is the preeminent figure in product datasheets concerning the steady-state thermal properties.

Had we this simplicity of the one-dimensional heat flow, the concept could be extended to stacked-chip structures (Figure 1) with some effort. Unfortunately, this simple picture no longer holds if we consider realistic structures with a three-dimensional (3D) heat flow. No single *junction temperature* can be defined if the temperature changes laterally on the chip, which is the typical case for multiple heat sources in multichip assemblies. The *case temperature* may exhibit even larger lateral variation at up-to-date packages, which are designed for high power and are usually rather flat. For example, dual cold plate assemblies and power packages with extended heat transfer features involving leads 124 lie beyond the scope of this linear thermal chain concept. In general, the junction-to-case thermal resistance concept is only applicable if – using the terminology of thermal modeling – an unambiguous "case thermal node" can be defined which finally absorbs all heat from the junction.

In this paper we shall first define how the concept of R_{th} thermal resistance can be extended to multichip and dynamic problems introducing a matrix of self- and transfer impedances. The concept will be demonstrated on measurements of

lateral multichip structures where transfer effects are strong. Then we outline inherent ambiguities of existing R_{thJC} measuring concepts based on Eq. (1) arising from the 3D heat flow, especially at the case surface. Afterwards we propose a transient characterization technique based on structure functions which allow to identify internal structures like die-attach and individual sample differences very clearly.

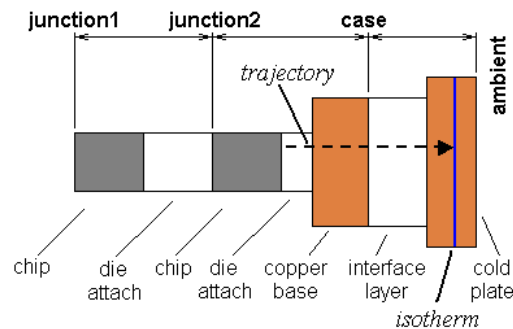


Figure 1. One dimensional model of the heat conduction path.

Finally we outline measurements on stacked-chip structures where additional thermal issues emerge related to the connection between top and bottom chip.

2. Multiport Modeling

A simple linear model of a multichip structure with a parallel Z_H heat conductance path is shown in Figure 2. Applying power P_1 and P_2 we experience T_1 and T_2 temperatures (relative to the ambient temperature) at the nodes J1 and J2.

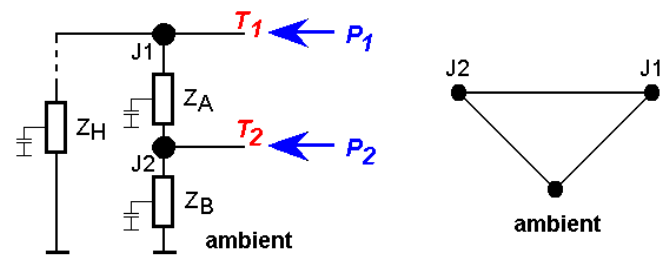


Figure 2. Simple model of a multichip structure.

This multiport structure can be characterized by applying P_1 and P_2 powers one-by-one. Exciting only J1 we can define:

$$T_1 = Z_{11} \cdot P_1, \quad T_2 = Z_{12} \cdot P_1 \quad (2)$$

Z_{11} is the self-impedance of the J1-ambient port, Z_{12} is the transfer impedance from the J1-ambient to the J2-ambient port. With the shorthand notation $A \times B$ for $A \cdot B/(A + B)$ we can write

$$T_1 = Z_{11} \cdot P_1 = Z_H \times (Z_A + Z_B) \cdot P_1 \quad (3)$$

$$T_2 = T_1 \cdot Z_B / (Z_A + Z_B) = Z_H \times (Z_A + Z_B) \cdot P_1 \cdot Z_B / (Z_A + Z_B) \quad (4)$$

Resolving the \times operations we get

$$T_2 = Z_H \cdot Z_B / (Z_H + Z_A + Z_B) \cdot P_1 \quad (5)$$

and so from (3) and (5)

$$Z_{11} = Z_H \times (Z_A + Z_B) = Z_H \cdot (Z_A + Z_B) / (Z_H + Z_A + Z_B) \quad (6)$$

$$Z_{12} = Z_H \cdot Z_B / (Z_H + Z_A + Z_B) \quad (7)$$

For very high Z_H values we get the obvious results

$$Z_{11} = Z_A + Z_B, \quad Z_{12} = Z_B \quad (8)$$

The graph of **Figure 2** is symmetric, if we excite only J2 we get Z_{22} and Z_{21} swapping Z_H and Z_B in (6) and (7):

$$Z_{22} = Z_B \times (Z_A + Z_H) = Z_B \cdot (Z_A + Z_H) / (Z_H + Z_A + Z_B) \quad (9)$$

$$Z_{21} = Z_H \cdot Z_B / (Z_H + Z_A + Z_B) \quad (10)$$

The network complies the reciprocity principle, $Z_{12} = Z_{21}$.

For very high Z_H values we get now

$$Z_{22} = Z_B, \quad Z_{12} = Z_B \quad (11)$$

It has to be noted that we can mathematically compose a quantity

$$Z_{\text{odd}} = Z_{11} - Z_{12} \quad (12)$$

Z_{odd} has no physical meaning and does not yield the value of Z_A as sometimes stated. Z_H can be neglected very rarely, even not in cold-plate setups. In many cases (e.g. wire bond PBGA package with heat sink) it is in the same order as Z_B . How we can get rid of the effect of unwanted parallel impedances is well written in 5.

3. Multichip Measurements in Lateral Structures

In stacked structures self- and transfer impedances can be of different magnitude, so we selected a lateral multichip structure initially, where these effects are very pronounced.

Example I. Infineon's BTS 7810 K quad DMOS switch device is a trilithic chip assembly in a P-TO263-15-1 package with one double high-side switch in the center and two low-side switches at the sides. The three vertical DMOS chips are mounted on separated leadframes. Figure 3 shows the package and its footprint outline with heatslugs H1, H2, and H3.

The first measurement was done on a JEDEC standard board in still-air chamber. After switching off a constant power dissipation P_1 at the device mounted on H1 we captured temperature transients of all devices.

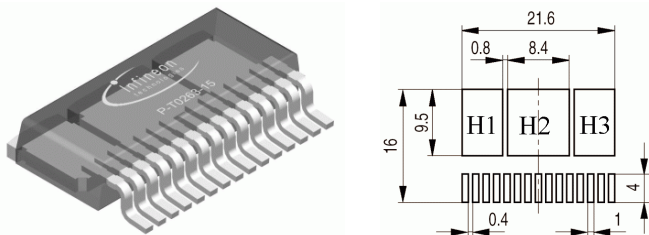


Figure 3. P- TO263-15-1 package , internal leadframes, footprint and heatslug numbering (H1, H2, H3).

In Figure 4 we show junction temperature curves fitted at their cold end. The curves are also scaled in Z_{th} :

$$Z_{11}(t) = -[T_1(t) - T_A] / P_1, \quad Z_{1k}(t) = -[T_k(t) - T_A] / P_1$$

For short times until 3 to 5 s (junction 2) or 12 s (junction 3), we see that the remote positions do not yet respond to the stopping of heat dissipation at junction 1. In the 100 second range all junctions have almost identical temperature and behave as a single heat source.

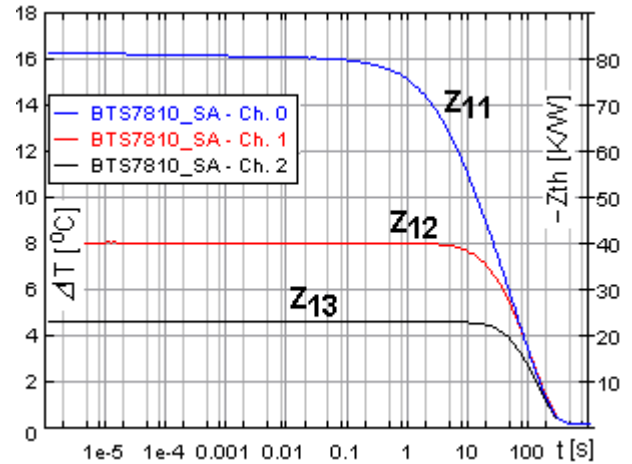


Figure 4. Z_{th} curves of a three-chip module in still air setup, self-heating and transfer, fitted to their final steady-state end.

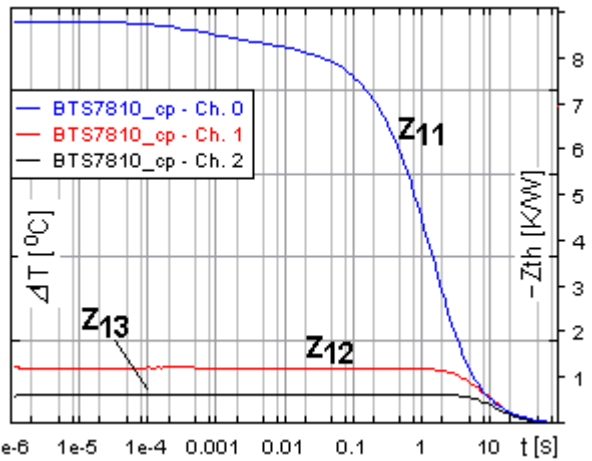


Figure 5. Z_{th} curves of a three-chip module, cold-plate setup.

In the next experiment we put the same device on a cold plate. In this setup the Z_{11} local temperature response to heating at junction 1 is much smaller (about 10%), and the steady-state is reached about one decade faster. As most heat flows directly to the cold plate, we observe drastically smaller transfer impedances for the junctions 2 and 3 (Figure 5).

As periodic excitations are typical for power switching devices, it is helpful to study the complex loci (Nyquist diagrams) in frequency domain. The $Z(\omega)$ complex impedances (Figure 6, Figure 7) are automatically calculated from time transients in the evaluation program of the transient tester. The excitation and the response can be decomposed into a sum of DC bias and sinusoidal components. The DC component can be read at very low frequencies. For the still-air setup we obtain the values 81, 40, and 23 K/W for steady-state Z_{11} , Z_{12} , Z_{13} , respectively. Coupling between the chips quickly diminishes at higher frequencies where the heat can be stored in

the mass of the own heatslug and does not reach the other chips in the package.

For the cold-plate setup, we find values of 8, 1.2, and 0.6 K/W for the low-frequency limits of $Z(\omega)$ corresponding to the strong decoupling of the chips. This is also reflected in the transient Z_{th} plots (cf. Figure 4, Figure 5).

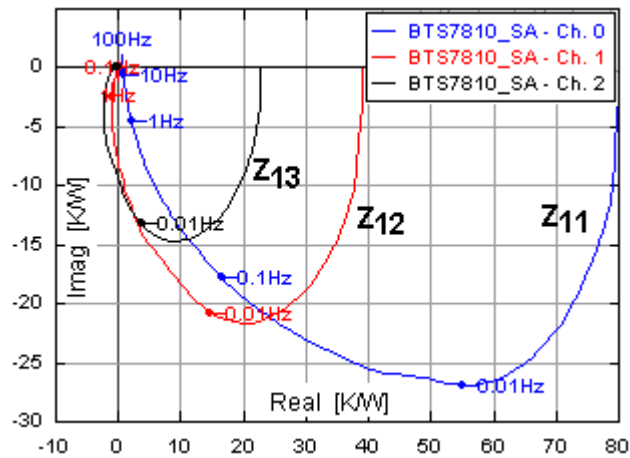


Figure 6. Self-impedance and transfer impedance curves for the three-chip module in still-air setup, complex loci.

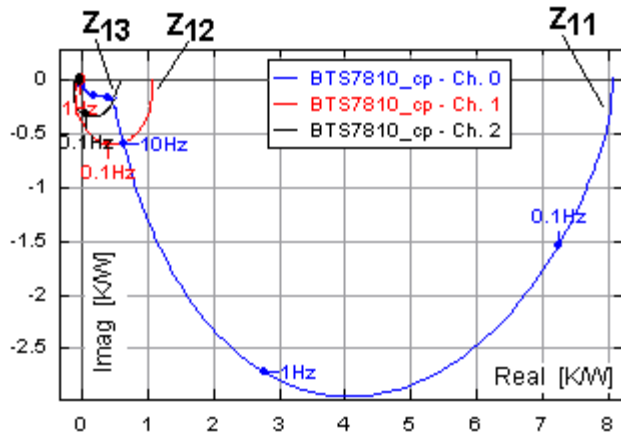


Figure 7. Self-impedance and transfer impedance curves for the three-chip module in cold-plate setup, complex loci.

Figure 8 repeats the complex loci of Figure 6 with junction 1 over H1 driven (Z_{11} , Z_{12}) and adds two measured complex curves with junction 2 over H2 driven (Z_{22} , Z_{21}). The expected reciprocity of transfer impedances can be well observed, although H1 and H2 are not symmetric (Figure 3).

It is worthwhile composing a full impedance matrix of all Z_{kn} elements. This is the metric that corresponds to the concept of R_{th} for multichip packages when the matrix contains DC values only. Giving the full set of $Z_{kn}(\omega)$ loci we extend the R_{th} concept to dynamic modeling.

4. The Junction-to-Case Problem

In the previous section we implicitly supposed that the junctions have uniform temperature. We can measure this temperature (or some average of the actual distribution) by the tester equipment and so we get the Z_{kn} values towards ambient or between temperature sensitive structures directly.

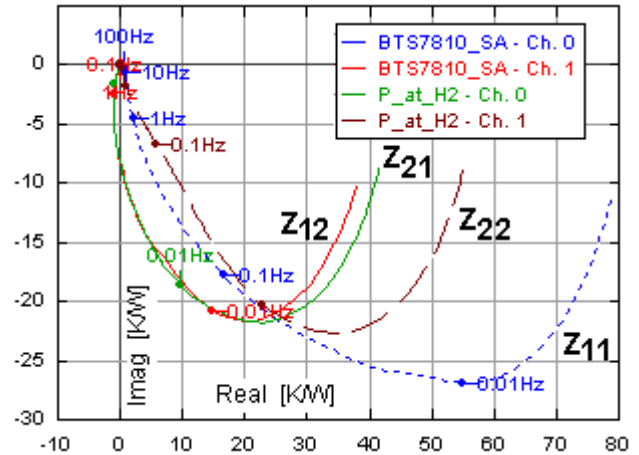


Figure 8. Comparison of complex loci in still-air setup. Curves Z_{11} , Z_{12} measured with junction on H1 driven, Z_{22} , Z_{21} measured with junction on H2 driven.

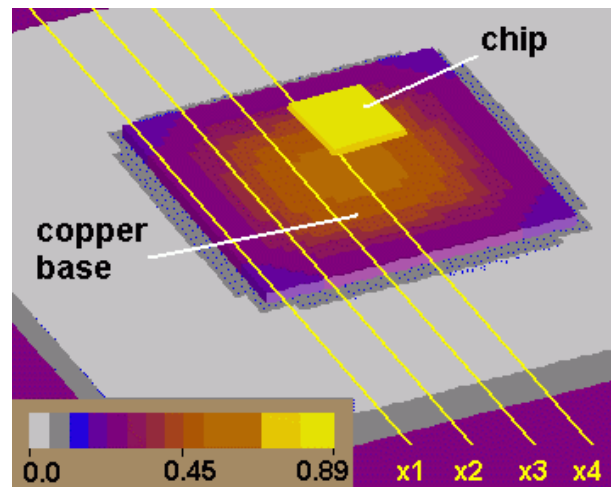


Figure 9. Simulation results of a MOSFET device on cold plate. Temperature distribution on the bottom of the copper base.

At packages having a large cooling surface (tab, heatslug) assuming uniform temperature is obviously unacceptable. On the other hand, the case surface is not temperature sensitive. Applying a large number of sensors on the case surface is impractical, and would distort the temperature field.

Below we present a simple and accurate approach based on temperature transients and demonstrated on simulation and measurements.

Example II. We selected an SPP80N06S2L-11 high power MOSFET in TO-220 package. For junction-to-case measurements one mounts the device on a cold plate and ap-

plies thermal grease on all surfaces to ensure good thermal contact.

We simulated the device on a cold plate at 1 W powering by a thermal simulator 6 to estimate the ambiguity of definition (1). As Figure 9 shows we obtain a total junction-to-ambient resistance R_{thJA} value of 0.89 K/W (interpreting "ambient" as the end of the cold plate). However, the temperature of the copper base shows much variation.

Plotting temperatures along different cross sections at the "case" plane (Figure 10) we experience changes between 0.1 and 0.28 °C, i.e. we cannot deduce a well-defined R_{thJC} according to (1). With $T_J = 0.89$ °C we can state that R_{thJC} varies between 0.61 and 0.79 K/W – a 30% variation, which is also expected in a real experiment depending on where T_C is measured.

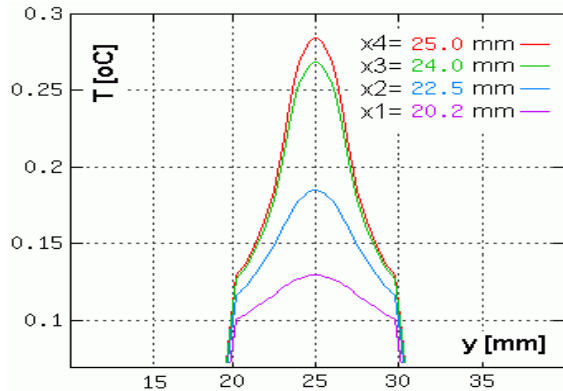


Figure 10. Plot of the temperature distribution along different cross sections at the bottom of the copper base.

From the theoretical point of view, the proper way to characterize the package would be to define concentric thermal nodes instead of a single case point. Also a multiport compact model with thermal resistances connecting the junction node to the bottom nodes and the latter to each other would give an acceptable result 7.

In practice, however, a device datasheet without a reproducible key parameter like R_{thJC} is not acceptable. As it turns out in the next section it is still possible to define such a parameter based on a transient measurement technique. Such a simple amount also offers advantages when comparing different devices.

5. Transient Measurements for Single MOSFET Devices

In the steady state technique, R_{thJC} is calculated from the endpoints of a cooling curve by taking the difference between the initial temperature at the junction (T_J) and the final temperature of the case surface (T_C), after switching off a constant power dissipation at the junction. T_J is determined from a calibrated temperature-sensitive parameter as the forward voltage of a diode, T_C may be measured by a thermocouple located in the cold plate beneath the device. Figure 11 illustrates a cooling curve, showing the junction and cold-plate temperatures vs. time.

This method adds the grease interface (and some of the cold plate) to the measured thermal resistance. In the transient and frequency domain we face additional problems. Figure 12 shows an RC model of the package, with a single junction

node and more nodes corresponding to different case locations, one of which is used for temperature probing. Comparing this figure to Figure 2 besides Z_A and Z_B we can also identify Z_H as the parallel impedance composed of all threads except the one where probing occurs. Dividing the temperature curves by P_1 in Figure 11, T_J can be scaled to Z_{11} , T_C to Z_{12} . The curve composed as $-(T_J - T_C)/P_1$ will correspond to Z_{odd} defined in (12). Z_{odd} has no physical meaning and is not monotonous. This is discussed shortly in 8 and more detailed in 9 but only an ad-hoc solution is proposed.

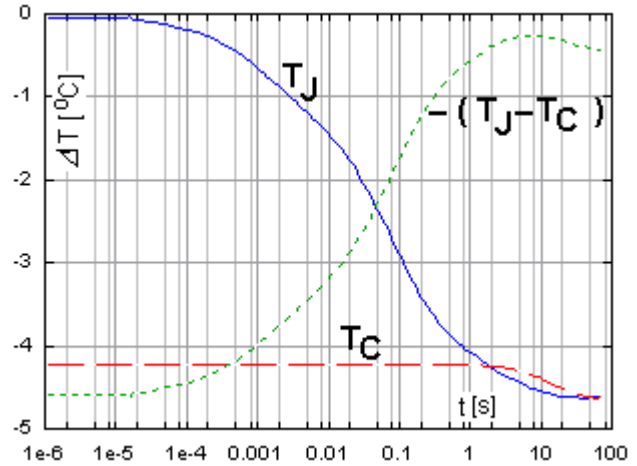


Figure 11. Cooling curves from traditional R_{thJC} measurements.

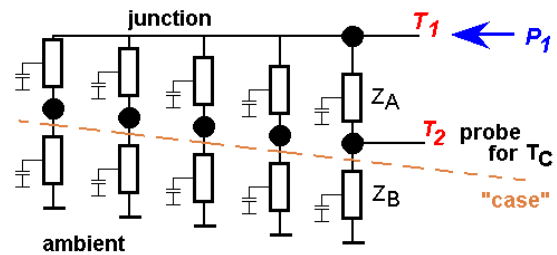


Figure 12. RC model of the junction-to-case problem.

Moreover, depending on the probing position we always get different temperature values due to the lateral temperature variation on the case surface. Small lateral displacements can cause 15% variation in the obtained R_{thJC} value.

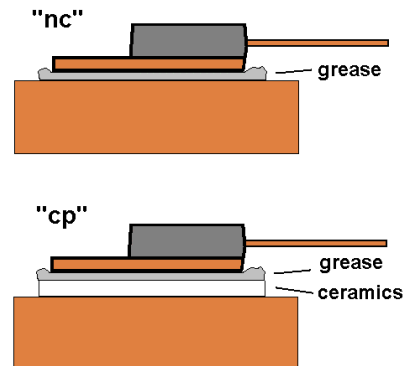


Figure 13. TO-220 package on cold plate: "nc" – directly attached; "cp" – with ceramic inlet.

Here we propose a transient characterization method, which yields more appropriate information about the thermal properties (and the device structure in detail), by comparing the measured and calculated curves belonging to two different setups, i.e. boundary conditions. To this end we have measured the transient junction temperature of power MOSFET devices in a TO-220 package with two boundary conditions (cf. Figure 13), without explicit measurement of the temperature at any place at the case surface:

- *Boundary condition "nc"*: Package pressed directly against cold plate;
- *Boundary condition "cp"*: Package pressed against a thin ceramics substrate placed on the cold plate.

In Figure 14 we can compare three transients of one sample in both setups, fit at their cold end. The repeatability is very high, the difference among the curves belonging to one setup is less than 2%. In Figure 15 we fit the curves at their hot ends. We observe that for the first 30 ms different boundary conditions yield the same curve, the heat propagates still in the package. Making the difference between the hot point and the temperature where the curves depart we can already say that R_{thJC} is slightly more than 0.6 K/W.

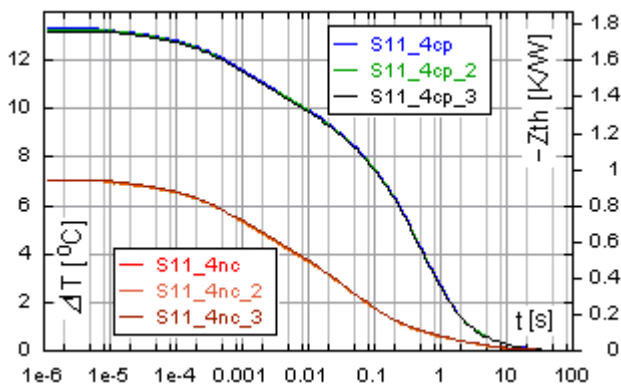


Figure 14. Cooling curves of a packaged power MOS in "nc" and "cp" setup, fit at the cold point.

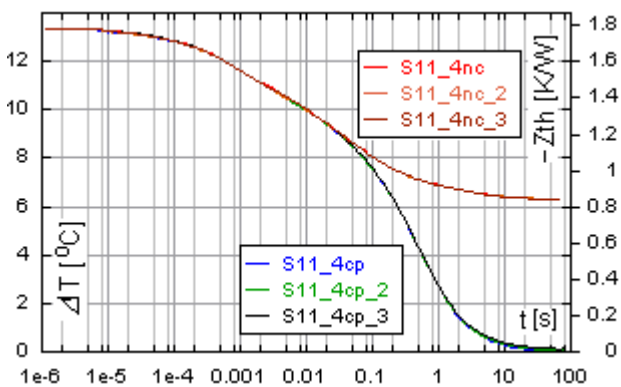


Figure 15. Cooling curves of Figure 14, fit at the hot point.

6. Structure Functions

For accurate description of thermal self-impedances we often calculate an equivalent 1D thermal RC network. At a large number of RC stages it is convenient to use a graphic representation, the structure functions 1011, where the *cumulative thermal capacitance* C_{Σ} is plotted as a function of the *cumulative resistance* R_{Σ} (Figure 16). Figure 17 shows the cumulative structure functions derived from the transients in Figure 14 and Figure 15. Steep sections correspond to material regions of high thermal conductivity or large cross-sectional area.

It is easier to identify the interface between the sections by looking directly at the $K(R_{\Sigma}) = dC_{\Sigma} / dR_{\Sigma}$ *differential structure function* (Figure 18) 12.

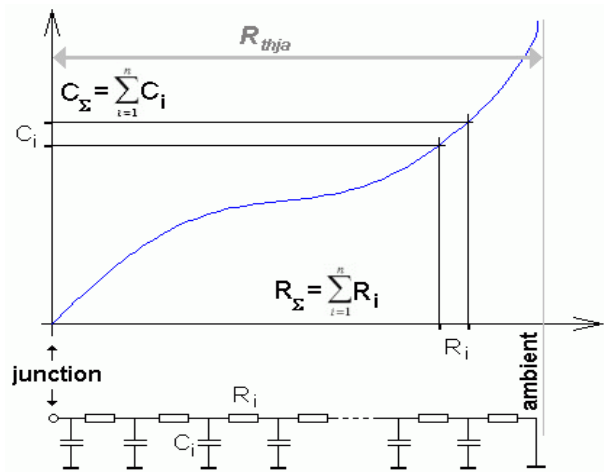


Figure 16. Cumulative structure function: the graphic representation of the thermal RC equivalent of the system.

Here peaks correspond to regions of high thermal conductivity like the chip or a heat sink and valleys show regions of low thermal conductivity like die attach or air 1314.

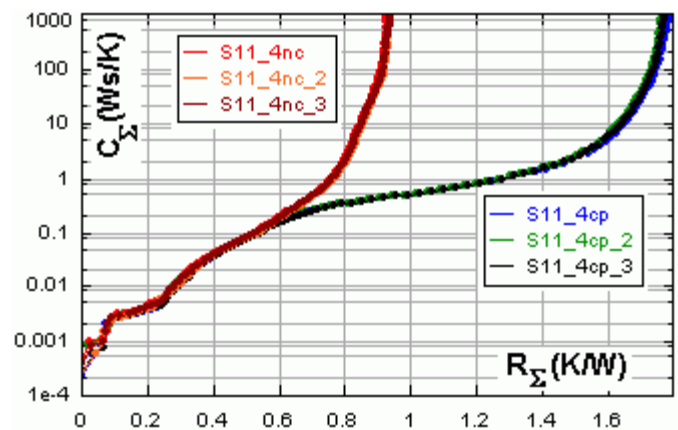


Figure 17. Cumulative structure functions of a device in cold plate setup calculated from the curves in Figure 15; with ceramics ("cp") and without ceramics ("nc").

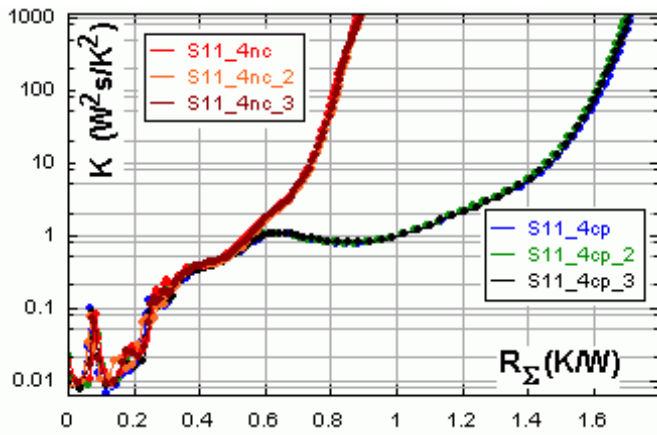


Figure 18. Differential structure functions of the device in cold plate setup.

Interface surfaces are represented as inflexion points of $K(R_\Sigma)$ between peaks and valleys. As pointed out in 15, this clear picture needs to be modified when the heat flow is no more one-dimensional; R_{th} values can be interpreted as single numbers only between isotherms, along trajectories. The interface planes show lateral R_{th} value variations, as demonstrated by simulation results in Figure 20.

Structure functions of 1D structures show sudden changes at the material interfaces. If we sum up thermal capacitances ($\leftarrow C_\Sigma$) in a narrow tube along a trajectory between two isotherms we get different cumulated C_Σ values belonging to the same R_Σ . In a thread near the center, the trajectory contains less copper and more grease or ceramics in a certain R_{thJC} interval thus the contribution to C_Σ is less than around the edges. In our present example the last peaks in the differential structure functions (Figure 18) at 0.62 K/W correspond most likely to the bulky copper base region. Afterwards we see the transition from copper to ceramics between 0.6 and 0.8 K/W along a flat curve. In the case of grease interface between copper base and cold plate we can't see pronounced peaks or valleys in Figure 18 but a rolling curve with inflexion points at the interfaces copper–grease and grease–cold plate at 0.67 K/W and 0.75 K/W (for details see also Figure 19).

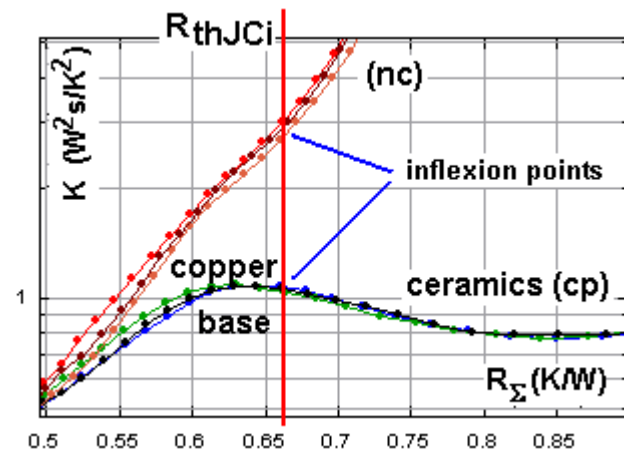


Figure 19. Detail of the differential structure function in Figure 18.

As proposed previously 15, we derive a parameter R_{thJCi} determined from the *point of maximum curvature* in the cumulative structure function, or the *inflexion point* of $K(R_\Sigma)$, in the region of the supposed interface from copper base to cooling mount (grease or ceramics in our example). This gives back exactly the geometrical interface planes in the 1D model of Figure 2 and can be considered as best approach for 3D heat flow. We obtain R_{thJCi} values around 0.66 K/W with 2–3% repeatability when comparing different samples and setups (Figure 19).

It has to be noted that from the R_{th} values in “nc” and “cp” setups also the *heatflux* through the ceramics can be calculated knowing the case area.

Measurement results were cross-validated by simulation. Simulated transients resembled the measured curves well. Figure 20 shows steady-state simulation results of the device on cold plate. R_{thJCi} approximately corresponds to the -0.65 K/W isotherm (if the junction is considered 0 K/W). It is important to note that this isotherm is not related to the geometrical case surface in any manner.

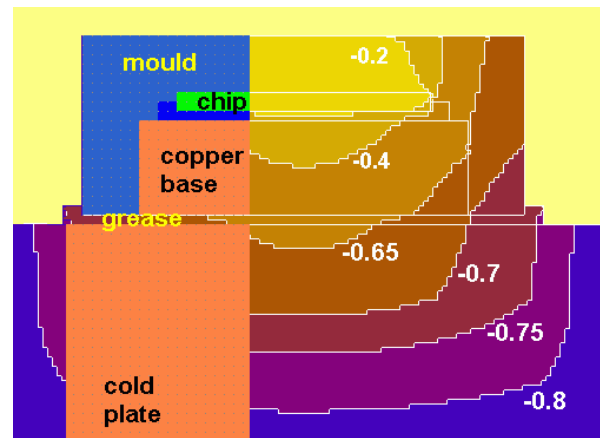


Figure 20. 3D simulation results of the packaged device on cold plate with isotherms (equidistant mesh, trajectories not shown). R_{thJCi} approximately corresponds to the -0.65 K/W isotherm.

Structure function methodology enables us to look also in the fine details of the structure. Figure 21 compares three MOSFET samples. We can attempt to find the chip region and die attach using the dimensions of the chip from Table 1. This gives a thermal capacitance of 1.95 mm^3 -silicon of about $C_{th} = -0.0032 \text{ Ws/K}$. We find this C_Σ value after 0.1–0.2 K/W in Figure 21, depending on the sample. The capacitance does not increase much until 0.25 K/W, i.e. in this section there is a material of low thermal conductance or cross section. This applies to the lead-based die-attach with less than 20% of the silicon specific heat.

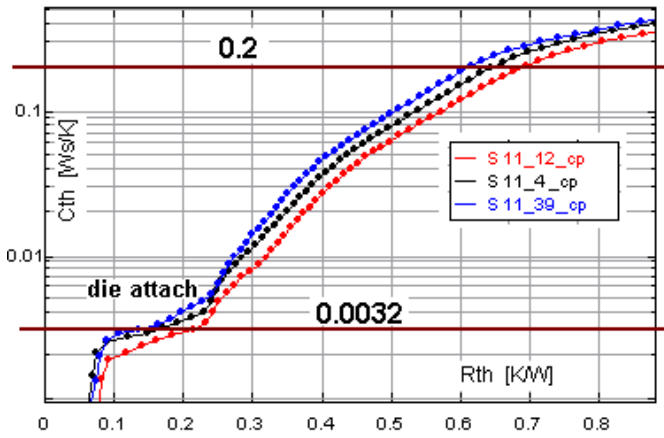


Figure 21. Cumulative structure function: Comparison of three MOSFET samples (4, 12, 39) with ceramics setup.

a (mm)	b (mm)	d (mm)	A (mm ²)	V (mm ³)	C_{th} (Ws/K)
3.27	3.40	0.175	11.12	1.95	0.0032

TABLE 1: Dimensions and thermal capacitance of the silicon chip with specific heat $C_{Si} = 0.703$ kJ/(kg K).

Dots in the structure function of the figure correspond to RC stages of Figure 16. The end of the die-attach region is clearly indicated by a sharp increase of the structure function beyond 0.25 K/W. Differences between samples develop in the die attach region, all curves run parallel afterwards.

This difference in die-attach quality can be verified by ultrasonic microscopy (Figure 22, using a 75 MHz transducer) where samples no. 4 and 39 exhibit thinner solder thickness and greater die tilt. Die tilt (i.e. varying solder thickness) shows up as an interference pattern in the ultrasonic echo signal (dark–bright transitions) which is most evident for part 39. The white spots are solder voids, here considered being of minor importance regarding the thermal resistance.

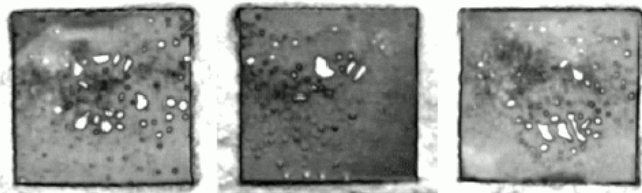


Figure 22. Ultrasonic images of the lead-based die-attach of the three devices in Figure 21, no. 4 (left), 12 (center), 39 (right).

The reduced solder thickness can be verified from the return times of the echoes. It correlates with reduced thermal resistances of the die attach compared with sample 12: the latter part has a more homogeneous and thicker solder layer yet a larger thermal resistance (Figure 21). Inhomogeneity in solder layer thickness (a 3D effect!) shows up as variation in the slope of the structure function in the die-attach region.

We can see that the cumulative structure function of all samples starts bending just after $C_{\Sigma} = 0.2$ Ws/K. Introducing the term R_{thJC} for R_{Σ} read at this fixed C_{Σ} value we slightly

underestimate the equivalent one-dimensional R_{thJC} defined by the maximum curvature, but we get excellent repeatability, because here all trajectories still run in the copper. At R_{Σ} values near to the bending some trajectories cross the case surface and actual grease width and attachment force influence the structure functions. Below the bending, we obtain the same ΔR_{th} difference within approximately $\pm 1\%$, regardless of the particular value of C_{Σ} chosen for reading-off R_{thJC} .

7. Measurement of a Vertical Multichip Structure

Additional features arise when we analyze the vertically stacked-chip architecture (chip-on-chip systems) where the heat from the top chip must flow through the bottom chip and the mold compound with low thermal conductivity.

Example III. We studied the thermal parameters of a BTS6143 device in TO252 like package. Here a small control chip is placed on top of a large power chip. **Figure 23** shows the draft geometry and the silicon structures we could use for excitation and sensing (reverse diode in the power chip, protection diode and a resistor separating the supplies in the control chip).

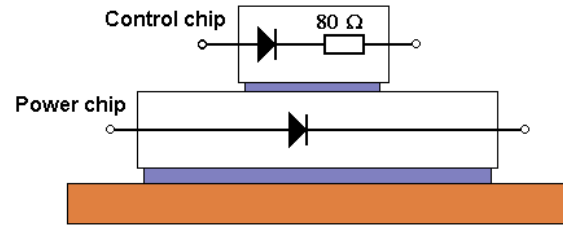


Figure 23. Stacked-chip system BTS6143.

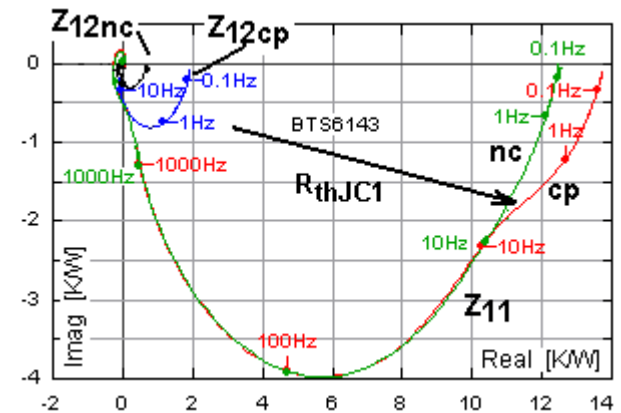


Figure 24. Complex loci of BTS6143, control chip driven.

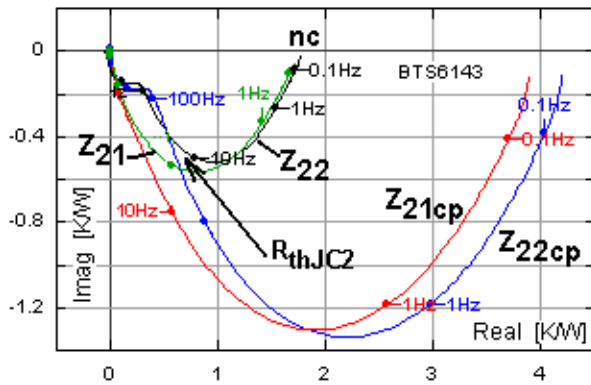


Figure 25. Complex loci of BTS6143, power chip driven.

We measured thermal transients and calculated complex loci in “nc” and “cp” setups of Figure 13 powering first the upper chip (Figure 24) then the lower chip (Figure 25). We can make many informative observations like:

- at pumping frequencies above 10 Hz the sinusoidal heat flow does not reach the case surface; self- and transfer impedances are independent from the setup;
- the control chip-to-case R_{th} is slightly more than 11 K/W, here Z_{11cp} and Z_{11nc} depart;
- the power chip-to-case R_{th} is approximately 0.7 K/W, here Z_{22cp} and Z_{22nc} depart;
- in the “cp” setup the parallel heat conduction path cannot be neglected even when the lower chip is excited, Z_{22cp} and Z_{21cp} differ;
- the structure is non-reciprocal, Z_{12} and Z_{21} curves differ. This can be easily explained: In the previous case of the lateral arrangement, the heating and sensing silicon structures are far from each other and can be treated as point-like entities from this distance. In the present case, Z_{12} depicts the response of the large lower chip on the heatflow from the 80 Ω resistor in the small upper chip. Z_{21} shows the response of the protection diode of the small upper chip on the heatflow from the whole surface of the large lower chip.

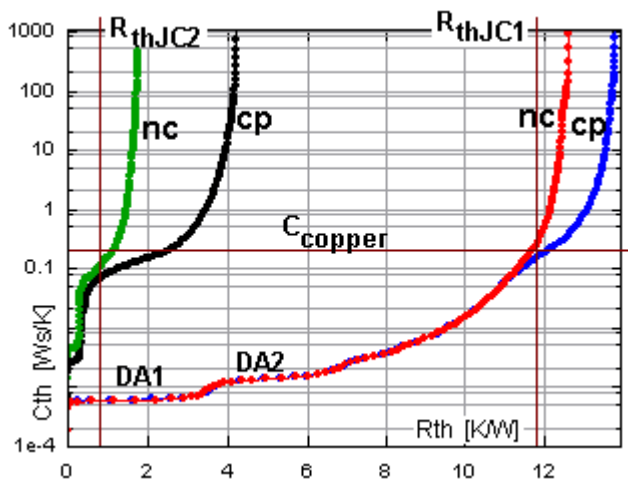


Figure 26. Cumulative structure functions of BTS6143, left to right: power chip excited in nc and cp setups, control chip excited in nc and cp setups.

In Figure 26 we see all cumulative structure functions. We can identify the DA1 and DA2 die attach regions in the curves belonging to the excited control chip. C_{th} is very low and R_{th} is very high in these sections as the heat propagates in a narrow cone below the control chip only.

The curves belonging to the power chip quickly turn into the characteristic shape of spreading in a copper cone under the large chip surface at a high capacitance value. Stepping into the cold plate occurs at similar C_{copper} value in all curves.

Reading the highest curvature (or inflexion of the derivative) in the curves we get 0.72 K/W for R_{thJC2i} and 11.7 K/W for R_{thJC1i} .

8. Conclusions

An impedance matrix of DC self- and transfer impedances can be used as a metric that corresponds to the concept of R_{th} for multichip packages. Extending this concept to a set of $Z_{kn}(\omega)$ complex loci we get a similar metric for dynamic modeling.

Elements of this matrix can be directly gained from thermal transient measurements.

We analyzed the case surface temperature distribution of high-power packages showing a characteristic three-dimensional heat flow. We found that the R_{thJC} junction-to-case thermal resistance cannot be interpreted as a single value due to the lateral temperature variation on the case surface.

We proposed an unambiguous definition for the R_{thJC} junction-to-case thermal resistance of such packages based on structure functions and presented a measurement technique ensuring high repeatability also at very low R_{th} values.

Selecting characteristic points on the structure functions we could use the results for die-attach quality analysis and for measuring the differences of R_{th} values among samples with very high resolution.

For overall thermal performance of a package, it is the average case temperature across the cooling mount that matters, rather than the local temperature at a probing position; hence by using the structure function analysis to derive R_{thJC} , we find more likely relevant macroscopic package differences when comparing different samples than by local probing of the case temperature.

For the future, it is of great interest to verify the measured die-attach characteristics on a larger number of measurements.

Acknowledgment

The authors would like to acknowledge fruitful discussions with Heinz Pape and Dirk Schweitzer (Infineon) and support within the European cooperation project PROFIT [1].

References

1. C. Lasance: The European Project PROFIT: Prediction of Temperature Gradients Influencing the Quality of Electronic products, Proc. 17th SEMITHERM, San José, pp. 120–125 (2001).
2. D. Schweitzer, H. Pape: Thermal Impedance of Packages in Dual Cold Plate Environments, Proc. 7th THERMINIC, Paris, pp. 245–249 (2001).
3. D. Schweitzer, H. Pape: Thermal Transient Modelling and Experimental Validation of Power Packages,

- Proceedings 8th THERMINIC, Madrid, pp. 17–22 (2002).
4. M. Rencz et al.: A procedure to correct the error in the structure function based thermal measuring methods, Proceedings 20th SEMITHERM, San José, pp. 92–98 (2004).
 5. V. Székely, A. Páhi, M. Rencz: SUNRED, a new field solving approach. Proceedings of the Symposium on Design, Test and Microfabrication of MEMS/MOEMS, Paris, pp. 278–288 (1999). See also www.micred.com/sunred.html.
 6. D. Schweitzer, H. Pape: Boundary Condition Independent Dynamic Thermal Compact Models of IC Packages, Proceedings. 9th THERMINIC, Aix-en-Provence (2003).
 7. B. Siegal: An alternative approach to junction-to-case thermal resistance measurements, Electronics Cooling Magazine, vol. 7, no. 2, May 2001.
 8. [www.electronics-cooling.com/html/2001_may_a4.html]
 9. J.W. Sofia: Analysis of thermal transient data with synthesized dynamic models for semiconductor devices. IEEE Transactions. on Component Packaging & Manufacturing Vol. 18, no. 1, pp. 39–47 (1995).
 10. E.N. Protonotarios, O. Wing: Theory of nonuniform RC lines, IEEE Trans. on Circuit Theory, vol. 14, no. 1, pp. 2–12 (1967).
 11. www.micred.com/strfunc.html.
 12. V. Székely, Tran Van Bien: Fine structure of heat flow path in semiconductor devices: a measurement and identification method, Solid-State Elec. vol. 31, pp. 1363–1368 (1988).
 13. Poppe, V. Székely: Dynamic Temperature Measurements: Tools Providing a Look into Package and Mount Structures, Electronics Cooling Magazine, vol. 8, no. 2, May 2002 [www.electronics-cooling.com/html/2002_may_a1.html].
 14. M. Rencz, et al.: Determining partial thermal resistances with transient measurements and using the method to detect die attach discontinuities, Proc. 17th SEMITHERM, San José, pp. 15–20 (2002).
 15. P. Szabó, O. Steffens, M. Lenz, G. Farkas: Transient junction-to-case thermal resistance measurements of high accuracy and high repeatability, Proc. 10th THERMINIC, Sofia-Antipolis, pp. 145–150 (2004).